11th International Symposium on Turbulence and Shear Flow Phenomena (TSFP11)
Southampton, UK, July 30 to August 2, 2019

INVESTIGATION OF TURBULENT BUDGETS IN CHANNELS WITH SECONDARY MOTIONS INDUCED BY STREAMWISE-ALIGNED RIDGES

K. Schäfer, A. Stroh, B. Frohnapfel, D. Gatti

Institute of Fluid Mechanics,
Karlsruhe Institute of Technology,
Karlsruhe, Germany
kay.schaefer@kit.edu

INTRODUCTION

Secondary flows are spontaneously-occurring large-scale swirling motions normal to the direction of the mean flow, i.e. the primary flow. Even though Nikuradse observed secondary flow already in the 1930s in a turbulent duct flow experiment with a non-circular cross-section, the prediction of the behaviour of secondary motions remains unclear. Since secondary motions often arise in flows over heterogeneous surfaces, their better understanding is of great interest for environmental processes such as atmospheric flows over varying topography or engineering applications such as performance degradation due to deposits on wind turbine blades and aircraft wings.

According to the classification by Prandtl (1952), secondary flows are divided into first and second kind. The former occur in both laminar and turbulent flows, whereas the latter arise only in turbulent flows. Secondary flows of the Prandtl's second kind are caused by Reynolds stress gradients in non-axisymmetrical turbulent flows (Bradshaw, 1987), and their presence have been observed not only in non-circular and open channels, but also in flows over heterogeneously rough surfaces (Hinze, 1973). Recently, considerable efforts have been made in order to understand the governing parameters for the generation of secondary flows over surfaces with spanwise varying drag. These include several experimental studies (Vanderwel & Ganapathisubramani, 2015; Barros & Christensen, 2014) and numerical investigations (Anderson *et al.*, 2015; Stroh *et al.*, 2016; Chung *et al.*, 2018; Vanderwel *et al.*, 2019), in which variation of spanwise surface heterogeneity and arrangement is considered. Thereby, the main focus has been on surfaces consisting either of roughness stripes and ridges or imposed wall shear stress modulation. In all previous cases the authors reported a presence of large-scale vortical structures at the edges between low and high wall shear stress regions. For channel flows with streamwise aligned ridges it has been shown that the secondary flows are particularly pronounced at a spacing of around half the channel height, δ, occupying large parts of the channel cross-section.

Regarding the origin of secondary motions, Hinze (1973) hypothesized that the role of secondary flows is to transport turbulent kinetic energy from areas of excess production to areas of excess dissipation. These areas can have different locations, depending on the properties of the introduced inhomogeneity. Hwang & Lee (2018), who studied turbulent kinetic energy budgets in turbulent boundary layers with different secondary motions, elaborate further Hinze's conjectures and found that the rotational sense of secondary flows is determined by the local strength of the turbulent transport term.

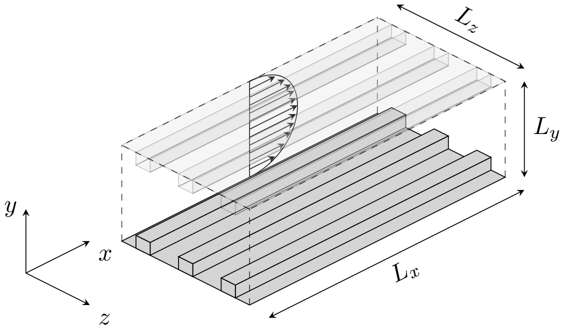

Figure 1: Schematic view of the numerical domain with streamwise elongated ridges.

In the present study we investigate the transport mechanisms of turbulent energy and different components of the Reynolds stresses in presence of secondary flows by means of the Reynolds stress budget equations. Secondary flows are generated via streamwise-aligned ridges with a constant element elevation and spanwise spacing, as shown in Figure 1.

METHODOLOGY

The analysis is carried out using flow fields produced via Direct Numerical Simulation (DNS) of fully-developed turbulent channel flows driven at a constant pressure gradient corresponding to the friction Reynolds number $Re_\tau = u_\tau \delta/\nu = 180$. $u_\tau = \sqrt{\tau_w/\rho}$ is the friction velocity and τ_w the average wall shear stress, while ν and ρ are respectively the kinematic viscosity and the density of the fluid. The simulations have been performed with the open-source code Incompact3d, employing sixth-order compact finite-differences for spatial discretization (Laizet & Lamballais, 2009; Laizet & Li, 2011). The governing equations are advanced in time via an explicit low-storage, third-order Runge-Kutta scheme. Continuity is imposed to machine

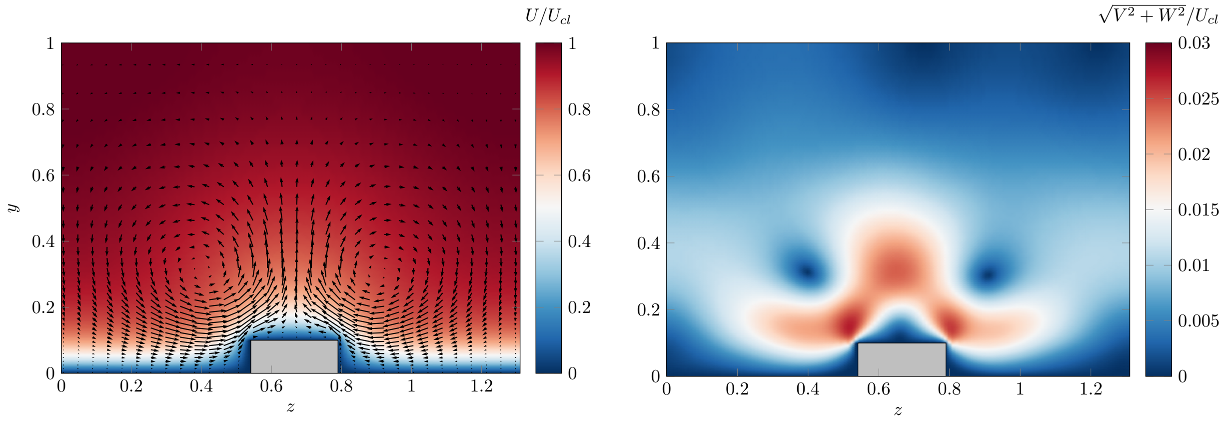

(a)

(b)

Figure 2: a) Contour of the phase-averaged streamwise velocity in the cross-section. The black arrows indicate the secondary motion normal to the main flow direction. b) Contour of the phase-averaged magnitude $\sqrt{V^2+W^2}$ of the secondary motion. All terms are normalized by the mean streamwise centerline velocity U_{cl}

Case	$N_x \times N_y \times N_z$	$L_x \times L_y \times L_z$	Δx^+	Δy^+_{max}	Δz^+	Re_τ	Re_b	C_f	U_b^+
smooth	$256 \times 129 \times 128$	$8\delta \times 2\delta \times 4\delta$	5.6	7.90	5.63	180	5654	$8.108 \cdot 10^{-3}$	15.71
structured	$256 \times 257 \times 384$	$8\delta \times 2\delta \times 4\delta$	5.6	3.95	1.88	180	5336	$8.762 \cdot 10^{-3}$	14.82

Table 1: Simulation parameters of the smooth and structured DNS case.

accuracy via fractional step method, in which the pressure correction is obtained by solving the pressure Poisson equation in spectral space. Periodic boundary conditions are applied in streamwise (x) and spanwise (z) directions, while the wall-normal (y) extension of the domain is bounded by no-slip boundary conditions at the lower and upper domain wall at $y = 0$ and $y = 2\delta$, where δ is the half channel height.

The surface structuring in form of a periodic spanwise array of streamwise-aligned ridges is introduced at both channel walls in a symmetric arrangement via the direct-forcing immersed boundary method proposed by Fadlun *et al.* (2000). The ridges protrude $H = 0.1\,\delta$ above the walls and have a spanwise width of $W = 0.25\,\delta$. The constant spacing between the centre of two ridges is $S = 1.33\,\delta$.

The turbulent channel flow with streamwise aligned ridges is compared with a smooth channel flow at the same value of Re_τ. The Cartesian grid of both simulations is equidistant in the streamwise and spanwise direction and in the wall-normal direction the grid points are distributed unevenly. For the structured simulation the wall-normal spacing is arranged in such a way that the first grid point from the wall is placed at $y^+ = 0.5$, where the superscript $^+$ indicates the non-dimensionalisation with wall units. Beside the number of grid points, which has been reduced to $N_x = 256$, $N_y = 192$ and $N_z = 192$ for the smooth channel simulation, all other discretisation parameters are kept same between the two simulations. The resulting flow properties and discretisation parameters are shown in table 1.

The velocity components in streamwise, wall-normal and spanwise directions are respectively denoted u, v, w, while p denotes pressure. Due to the periodic nature of the ridges, the phase-averaging operator for the generic flow quantity f is introduced

$$\langle f \rangle (y,z) = \frac{1}{N} \sum_{n=1}^{N} \int_t \int_x f(x,y,z+nS,t)\, \mathrm{d}t\, \mathrm{d}x\,, \tag{1}$$

while the respective Reynolds decomposition can be written as $f(x,y,z,t) = F(y,z) + f'(x,y,z,t)$. Capital letters $F = \langle f \rangle$ are used to indicate averaged quantities. The top and bottom half of the channel are averaged together exploiting the given statistical symmetry. In the flat wall case, phase-averaging along the spanwise direction reduces to standard averaging.

We analyse the Reynolds stress $\left\langle u_i' u_j' \right\rangle$ budget equations, which read

$$\begin{aligned} V \frac{\partial \langle u_i' u_j' v' \rangle}{\partial y} &+ W \frac{\partial \langle u_i' u_j' w' \rangle}{\partial z} \\ &= T_{ij} + P_{ij} + \Pi_{ij} + D_\nu + \varepsilon_{ij}\,, \end{aligned} \tag{2}$$

where T_{ij} is the turbulent transport of the Reynolds stresses, P_{ij} is the production, Π_{ij} corresponds to the velocity-pressure-gradient term, D_ν is the viscous transport of the Reynolds stresses and ε_{ij} is the viscous dissipation. The velocity-pressure-gradient term Π_{ij} of the Reynolds stresses can be decomposed into the pressure strain term

Π^s_{ij} and the pressure transport term Π^d_{ij}:

$$\Pi^d_{ij} = \frac{1}{\rho}\left(\frac{\partial\langle u'_j p'\rangle}{\partial x_i} + \frac{\partial\langle u'_i p'\rangle}{\partial x_j}\right), \qquad (3)$$

$$\Pi^s_{ij} = -\frac{1}{\rho}\left(\langle p'\frac{\partial u'_j}{\partial x_i}\rangle + \langle p'\frac{\partial u'_i}{\partial x_j}\rangle\right). \qquad (4)$$

Taking the trace of eq. 2 yields the turbulent kinetic energy k budget equation

$$V\frac{\partial k}{\partial y} + W\frac{\partial k}{\partial z} = P_k - \varepsilon_k + T_k + D_k + \Pi_k, \qquad (5)$$

in which the terms on the right hand side are defined as follows:

$$P_k = -\langle u'_i u'_j\rangle\frac{\partial U_i}{\partial x_j}, \qquad \varepsilon_k = \nu\langle\frac{\partial u'_i}{\partial x_j}\frac{\partial u'_i}{\partial x_j}\rangle,$$

$$T_k = -\frac{1}{2}\frac{\partial\langle u'_i u'_i u'_j\rangle}{\partial x_j}, \qquad \Pi_k = -\frac{1}{\rho}\frac{\partial\langle u'_j p'\rangle}{\partial x_j},$$

$$D_k = \nu\frac{\partial^2 k}{\partial x_j^2}.$$

P_k is the production, ε_k the dissipation, T_k the turbulent transport, Π_k the pressure transport and D_k the viscous diffusion of turbulent kinetic energy.

The ridges induce secondary motions visible as wall-normal (V) and spanwise (W) mean velocity components, which enable additional advection of Reynolds stresses (left hand side of eq. 2 and 5) otherwise not present in smooth channels. The spanwise inhomogeneity of the Reynolds stresses is a feature of flows with secondary motions. In the following the individual budget terms of the turbulent kinetic energy and the Reynolds stress equation are examined in the channel cross-section.

RESULTS

The mean streamwise velocity U in the cross section is presented in figure 2a for the channel with ridges. Arrows indicate the wall-normal V and spanwise W velocity components associated with the secondary motion, while the streamwise-elongated ridge is represented via a grey contour.

A clearly noticeable secondary flow occurs with large wall-normal and spanwise extent, which reaches up to the channel centreline. The upwash motion of slow fluid towards the bulk can be seen above the ridge structure, while a downwash of high velocity from the channel bulk towards the walls takes place in the valley between the ridges. The local magnitude of the secondary motion, defined as $\sqrt{V^2+W^2}$ is presented in figure 2b. The strength of the secondary flow amounts 2.68% of the mean centreline velocity. Even though the present Reynolds number is significantly lower, the strength of the secondary motions corresponds to the values reported in previous studies at higher Reynolds number (Vanderwel *et al.*, 2019)

In order to improve the understanding of the role played by he secondary motion in the transport of turbulent stresses, the focus will lie in the following on the budget terms of the turbulent kinetic energy and the Reynolds stresses.

In figure 3a the contour of the turbulent kinetic energy k is presented. There are two peaks in proximity of the corners of the ridge, which are related to the strong mean velocity gradients introduced by the protruded surface. These cause also a localised region of large production P_k (figure 3c). Furthermore, k exhibits a local maximum at the center of the valley between two consecutive ridges, which might be ascribed to the downwash caused by the secondary flow, which pushes high velocity fluid to the wall at the valley center.

The influence of turbulent transport T_k is visualised in the cross-section of the channel in figure 3b. High levels of T_k occur in the same spatial locations at which k is large. Qualitatively T_k exhibits the same behavior observed above flat channel walls: it withdraws energy from the buffer layer, where maximum production occurs, and deposits it in the vicinity of the wall and in the flow bulk. However, there are some important differences related to the presence of the ridges and the secondary motion. First, the peak positive value of T_k occurs close to the ridge wall where the advection of k associated with the secondary motion is also large. The large negative region of T_k with two local peaks further away from the ridge results in a non-negligible contribution to k present in the bulk region of the flow. Hence, the production P_k and dissipation ε_k, the two other main local contributors, are not in local equilibrium.

Figure 3c and 3d show P_k and ε_k respectively. As can be seen, the value of ε_k is particularly pronounced at the corners of the ridge with two strong peaks. The production P_k also shows two strong peaks, located slightly above the ridge, within the buffer layer, featuring a larger extent. The present results qualitatively agree with the boundary layer investigation by Hwang & Lee (2018).

In order to see how strong the influence of the secondary motion remains further away from the ridges, the budget terms of the turbulent kinetic energy at the center of the valley are presented in figure 4. The results obtained for the channel with ridges are compared with the smooth wall case. The values of P_k and ε_k are lower than in the plane channel flow throughout the whole channel height. It is confirmed that the turbulent transport is reduced close to the wall, but it plays a more dominant role for larger wall distances $y^+ > 30$, counteracting the effect of advection by secondary motions (see also figure 3b).

Gradients of Reynolds stresses are known to act as a source for the mean streamwise vorticity, thus contributing to the formation of secondary motions (Bradshaw, 1987). In order to understand how Reynolds stresses are produced and transported throughout the channel, we focus in the following on the Reynolds stress budget equations. In figure 5a and 5b the phase-averaged contours of the Reynolds stress $\langle u'v'\rangle$ and $\langle v'w'\rangle$ are presented. The maximum value of $-\langle u'v'\rangle$ is found above the ridge at the wall-normal position $y \approx 0.4$, while a second peak is found at the center of the valley. The contour of $\langle v'w'\rangle$ shows two strong opposite-signed peaks close at the corner of the ridge, reflecting the opposite flow direction of the secondary flow. The maximum amplitude of $\langle v'w'\rangle$ is lower compared to $\langle u'v'\rangle$, but the area of non-negligible $\langle v'w'\rangle$ largely extends throughout the channel.

The source term $P - \varepsilon + \Pi^d$, consisting of the production, dissipation and pressure strain, of the Reynolds stresses $\langle u'v'\rangle$ and $\langle v'w'\rangle$ are shown in figure 5c and 5d. Neither the contour of the source of $\langle u'v'\rangle$ nor the contour of the source of $\langle v'w'\rangle$ corresponds to the respective

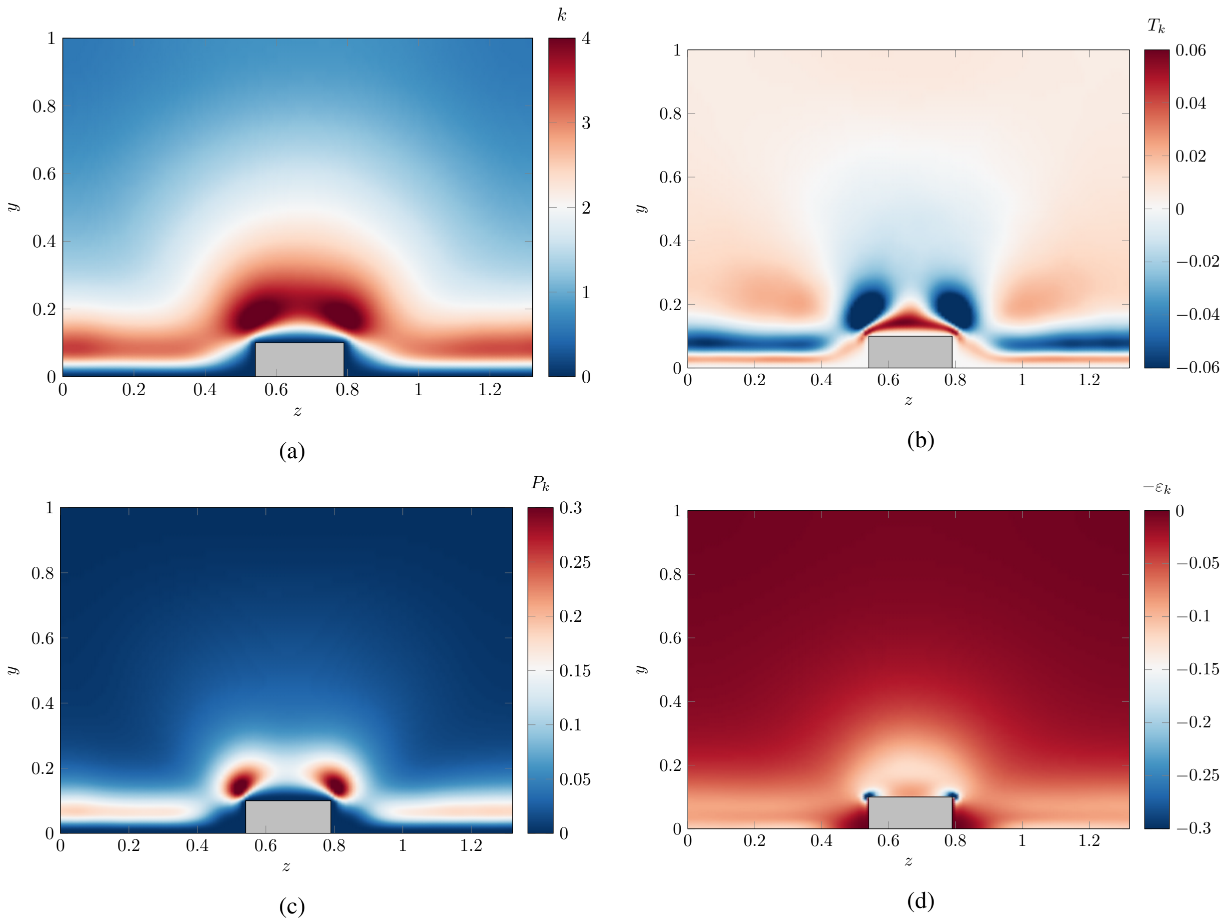

(a)

(b)

(c)

(d)

Figure 3: a) Contour of the phase-averaged turbulent kinetic energy in the cross-section. b) Contour of the turbulent transport of the turbulent kinetic energy T_k . c) Contour of the turbulent kinetic energy production P_k. d) Contour of the dissipation of turbulent kinetic energy ε_k. All budget terms are normalized by u_τ^4/ν.

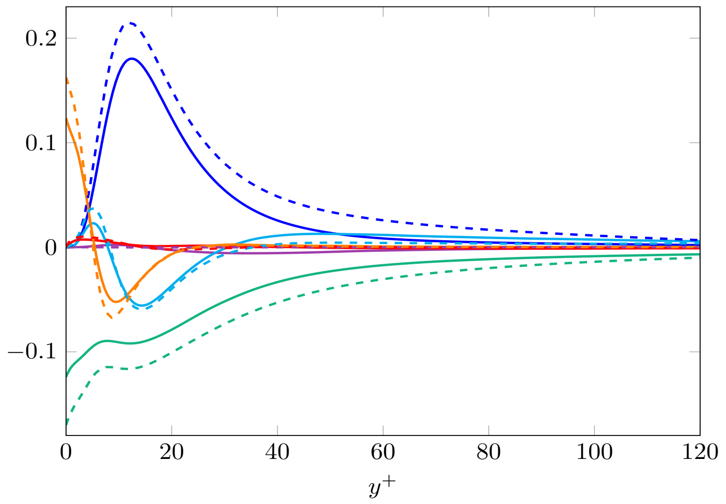

Figure 4: Budget terms of the phased-averaged turbulent kinetic energy k in wall coordinates at the valley center between two ridges normalized by u_τ^4/ν. Solid lines indicate the budget terms of the simulation with imposed ridges, while dashed lines indicate the budget terms of the plane channel simulation. The color of the lines representing: advection term —; production term P_k, —; turbulent transport T_k, —; pressure transport Π_k, —; viscous diffusion D_k, —; dissipation $-\varepsilon_k$, —.

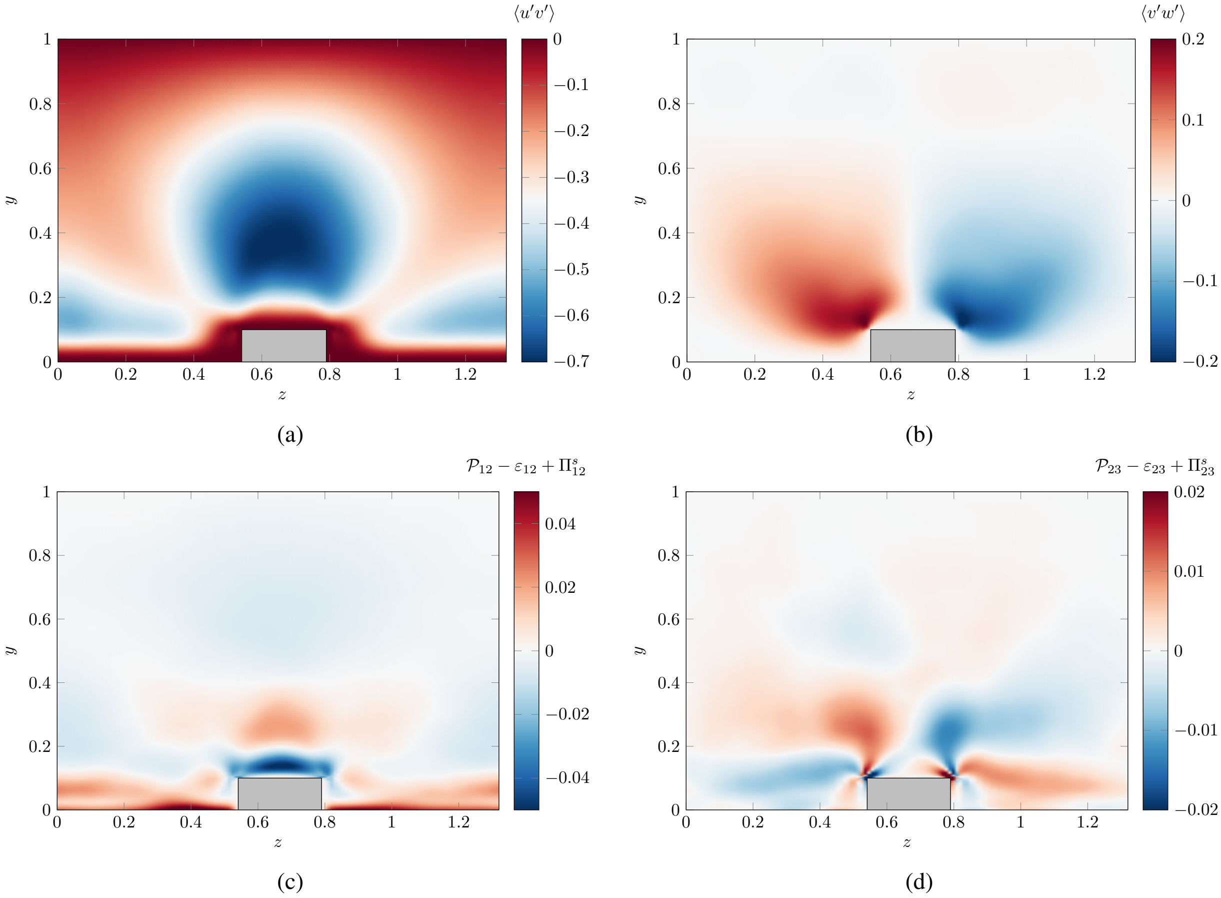

Figure 5: Contours of the phase-averaged Reynolds stresses for a) $\langle u'v' \rangle$ and c) $\langle v'w' \rangle$. Contour of the phase-averaged difference between the budget terms of production, dissipation and pressure strain for b) $P_{12} - \varepsilon_{12} + \Pi^s_{12}$ and d) $P_{23} - \varepsilon_{23} + \Pi^s_{23}$. All budget terms are normalized by u_τ^4/ν.

Reynolds stress counterpart, which indicates a strong influence of transport processes. While the source of $\langle u'v' \rangle$ shows a qualitatively similar behaviour to a smooth channel at the center of the valley, it is opposite above the ridge with a strong production (negative peak) occurring in the vicinity of the wall. This converse behaviour is related to the complex composition of the $\langle u'v' \rangle$-production and might originate from the locally strong spanwise mean velocity gradients.

The source term for $\langle v'w' \rangle$ depicts a more complex pattern. Maximum positive and negative values of the source are found close to the corner of the ridge. The positive contour extends upwards to the channel center with a pronounced lateral drift to the sides at around $y = 0.2$. From the highly negative values at the corner, the distribution of the $\langle v'w' \rangle$-source spreads laterally and encloses a small area of positive source, which flanks the ridges.

CONCLUSION & OUTLOOK

The current study investigates the production, transport, dissipation and advection of turbulent kinetic energy and Reynolds stresses in a turbulent channel with secondary flows induced by spanwise heterogeneous structured surfaces. The redistribution of Reynolds stresses related to the secondary motions significantly impacts the Reynolds stress budgets compared to a smooth channel flow. In particular, it has been observed that production and dissipation of turbulent kinetic energy deviate further from local equilibrium due to enhanced turbulent transport.

Further investigations will focus on the spectral analysis of the different budget terms, in order to better understand the scale-dependent contribution. Of particular interest is the turbulent transport term, which has the potential to highlight the nonlinear interaction of different scales and its contribution to the transfer between large and small structures. This might shed light on the turbulence modification caused by surface inhomogeneity and its relation to secondary motions.

ACKNOWLEDGEMENT

This work was performed on the supercomputer ForHLR and the storage facility LSDF funded by the Ministry of Science, Research and the Arts Baden-Württemberg and by the Federal Ministry of Education and Research. The support through the project Priority Programme SPP 1881 Turbulent Superstructures of DFG is greatly acknowledged.

REFERENCES

Anderson, William, Barros, Julio M., Christensen, Kenneth T. & Awasthi, Ankit 2015 Numerical and experimental study of mechanisms responsible for turbulent secondary flows in boundary layer flows over spanwise heterogeneous roughness. *Journal of Fluid Mechanics* **768**, 316–347.

Barros, Julio M. & Christensen, Kenneth T. 2014 Observations of turbulent secondary flows in a rough-wall boundary layer. *Journal of Fluid Mechanics* **748**.

Bradshaw, P. 1987 Turbulent secondary flows. *Annual Review of Fluid Mechanics* **19** (1), 53–74.

Chung, D., Monty, J. P. & Hutchins, N. 2018 Similarity and structure of wall turbulence with lateral wall shear stress variations. *Journal of Fluid Mechanics* **847**, 591–613.

Fadlun, E. A., Verzicco, R., Orlandi, P. & Mohd-Yusof, J. 2000 Combined Immersed-Boundary Finite-Difference Methods for Three-Dimensional Complex Flow Simulations. *Journal of Computational Physics* **161** (1), 35–60.

Hinze, J. O. 1973 Experimental investigation on secondary currents in the turbulent flow through a straight conduit. *Applied Scientific Research* **28** (1), 453–465.

Hwang, H. G. & Lee, J. H. 2018 Secondary flows in turbulent boundary layers over longitudinal surface roughness. *Physical Review Fluids* **3** (1).

Laizet, Sylvain & Lamballais, Eric 2009 High-order compact schemes for incompressible flows: A simple and efficient method with quasi-spectral accuracy. *Journal of Computational Physics* **228** (16), 5989–6015.

Laizet, Sylvain & Li, Ning 2011 Incompact3d: A powerful tool to tackle turbulence problems with up to O(105) computational cores. *International Journal for Numerical Methods in Fluids* **67** (11), 1735–1757.

Nikuradse, J. 1930 Untersuchungen über turbulente Strömungen in nicht kreisförmigen Rohren **1** (3), 306–332.

Prandtl, Ludwig 1952 Essentials of fluid dynamics. *Blackie and Son* **79** (342), 570–570.

Stroh, A., Hasegawa, Y., Kriegseis, J. & Frohnapfel, B. 2016 Secondary vortices over surfaces with spanwise varying drag. *Journal of Turbulence* **17** (12), 1142–1158.

Vanderwel, C. & Ganapathisubramani, B. 2015 Effects of spanwise spacing on large-scale secondary flows in rough-wall turbulent boundary layers. *Journal of Fluid Mechanics* **774**.

Vanderwel, C., Stroh, A., Kriegseis, J., Frohnapfel, B. & Ganapathisubramani, B. 2019 The instantaneous structure of secondary flows in turbulent boundary layers. *Journal of Fluid Mechanics* **862**, 845–870.